Journal of Structural Geology 201 (2025) 105559

Contents lists available at ScienceDirect

Journal of Structural Geology

journal homepage: www.elsevier.com/locate/jsg

Decoding microstructures of fault carbonate rocks with X-ray microtomography: A deep learning approach to fabric classification and analysis

Marco Voltolini [a,*], Luca Smeraglia [b], Andrea Billi [b], Eugenio Carminati [c], Flavio Cognigni [d,e,1], Marco Rossi [d,e], Michele Zucali [a]

[a] Dipartimento di Scienze della Terra "Ardito Desio", via Mangiagalli 34, 20133, Milano. Italy
[b] Consiglio Nazionale delle Ricerche, IGAG, P.le Aldo Moro 5, 00185, Roma, Italy
[c] Dipartimento di Scienze della Terra, Sapienza Università di Roma, P.le Aldo Moro 5, 00185, Roma, Italy
[d] Dipartimento di Scienze di Base e Applicate per l'Ingegneria, Sapienza Università di Roma, P.le Aldo Moro 5, 00185, Roma, Italy
[e] CNIS, Centro di ricerca per le Nanotecnologie applicate all'Ingegneria della Sapienza, Sapienza Università di Roma, P.le Aldo Moro 5, 00185, Roma, Italy

ARTICLE INFO

Keywords:
Fault
Fractures
Cataclasite
Breccia
Image processing
Machine learning
X-ray MicroTomography
Rock fabric

ABSTRACT

Fault zones in carbonate rocks exhibit distinct microstructural fabrics that develop different microstructures with increasing deformation, going from the outer zone towards the fault core. These fabrics can be effectively characterized using X-ray micro-computed tomography (XRμCT), a powerful imaging technique that supports a wide range of analyses, from morphometric measurements (e.g., pore size distribution, fractures orientation) to digital rock physics (i.e., virtual experiments on 3D volumes). However, the need for an automated, user-independent tool to classify these microstructures is crucial for large-scale studies. Furthermore, a fully quantitative classification of fault rock fabrics provides valuable insights into the extent and nature of deformation within these rocks. In this study, we present a deep learning-based supervised neural network designed to automate the classification of fault rock microstructures. This system offers rapid, quantitative, and scalable analysis of XRμCT data, facilitating the identification and classification of fabrics of brittle fault limestone rocks with high precision. The network was trained and validated on purpose collected datasets representing specific fabrics, then it was successfully used on different limestone fault rocks collected from the same area or obtained from the literature. The results show that the software can reliably classify fault rock fabrics affected by brittle deformation into three primary categories, each representing a distinct stage of deformation: fractured limestone, breccia, and cataclasite. The network assigns identification probabilities to each image, which can then be visualized in a ternary diagram for intuitive comparison and interpretation. This classification system streamlines fabric analysis and provides a quantitative measure of the degree of deformation within the rock. This automated classification tool paves the way for advanced studies on the anisotropic properties of fault rocks, enabling high-throughput analysis and enhancing our understanding of fault zone mechanics.

1. Introduction

Documenting the fabric of faults in carbonate rocks is crucial for both scientific and economic reasons. Faults can act as conduits or barriers for subsurface fluid migration, influencing crustal fluid budgets (e.g. Sibson, 1994), chemical reactions (e.g. Niwa et al., 2015), groundwater resources (Caine et al., 1996; Evans et al., 1997), CO_2 sequestration, and hydrocarbon reservoir entrapment (Ahr, 2011; Burchette, 2012; Annunziatellis et al., 2008; Lan et al., 2015; Mudry et al., 2002; Pérez-Lòpez et al., 2020; Wu et al., 2016; Zhiwen et al., 2020). For flow prediction, a characterization of fault rock microstructures -especially in terms of anisotropy, porosity, and hydraulic properties-is essential to assess hydrocarbon retention (Lucia et al., 2003; Rezaee et al., 2006), aquifer hydrogeology (Maclay and Small, 1984; Worthington, 1999) and CO_2 geological storage (Voltolini and Ajo-Franklin, 2019).

Before the assessment -or modeling-of hydraulic properties in fault

* Corresponding author.
E-mail address: marco.voltolini@unimi.it (M. Voltolini).
[1] Now at: Carl Zeiss S.p.A., Research Microscopy Solutions, Via Varesina 162, 20156 Milan, Italy.

https://doi.org/10.1016/j.jsg.2025.105559
Received 15 July 2025; Received in revised form 21 September 2025; Accepted 22 September 2025
Available online 23 September 2025
0191-8141/

rocks, a key step is a comprehensive and quantitative classification of the rock microstructure, and this work focuses on this first stage of the characterization of fault rocks. Documentation is typically time consuming, and classification is subject to application of rules that require expert knowledge (e.g., Mort and Woodcock, 2008). A promising direction is automated image collection and classification, an approach that has been proven successful for rock fabrics at both the micro- (Młynarczuk et al., 2013) and macro- (Zhang et al., 2018) scale, using different techniques for image acquisition. In this context, our study represents an important step forward in automated rock microstructure identification by introducing a deep learning-based approach to classify fault rock microstructures in limestones, using X-ray micro-computed tomography (XRμCT) data.

The development of an automated system for fault rocks microstructures classification using XRμCT datasets is especially appealing since it is possible to acquire a large amount of data relatively quickly, especially comparted to optical or electron microscopy, including automated systems. This large amount of data is a fundamental requirement for the training phase of machine learning (ML) procedures. Once a ML system has been successfully trained, its application, even on very large amounts of data (thousands -or more-images), is extremely fast. This study focuses on the automatic identification of fault rock microstructures, which directly informs specific procedures to be employed in any eventual morphometric or anisotropy analysis. However, the morphometric/anisotropy analysis itself is not covered within the scope of this work and will be addressed in a different publication.

Machine learning is a field of endeavor that enables computers to make successful predictions using past experiences. Given its rapidly growing capacity to handle complex, large, and heterogeneous datasets, recent advancements in machine learning (ML) have revolutionized multiple disciplines, including geosciences (Jordan and Mitchell, 2015; Zhong et al., 2021). The use of multi-layered neural networks, known as deep learning (DL), a subset of machine learning capable of automatically extracting patterns from data such as images (including microstructural textures commonly encountered in geosciences), had remarkable success in image-based classification tasks, as exemplified by widely used tools such as Google Images (Szegedy et al., 2015). DL architectures like GoogLeNet have been effectively employed across diverse domains, including medicine (Al-Huseiny and Sajit, 2021), robotics (Ak et al., 2022), computer vision (Anand et al., 2019), and satellite imagery (Shafaey et al., 2018). Novel applications of DL in the field of classification of microstructures include analysis of cultural heritage ceramics (Lyons, 2021), shales (Knaup, 2022), and carbonate rocks (dos Anjos et al., 2021). The image types of these studies include optical microscopy transmitted light images, backscattered scanning electron microscope images and XRμCT. Inspired by these successes, our work develops a DL-based tool capable of automatically classifying carbonate fault rocks and guiding the appropriate morphometric analysis to quantify their anisotropic properties.

The significance of our approach is particularly evident when comparing it to traditional methods. Currently, fault rock classification relies on human expertise (Sibson, 1977; Wise et al., 1984; Caine et al., 1996; Woodcock and Mort, 2008), which like other geological classification methods likely gives varying results (e.g. Andrews et al., 2019). Operator subjectivity and experience influence classification, particularly in samples with ambiguous microstructures. A quantitative approach based on morphometric parameters is desirable but remains challenging due to the complexity of fault rock textures and the expertise required for accurate interpretation, especially through optical and electron microscopy techniques. DL approaches offer the advantage that, once sufficiently large training datasets have been assembled and a model has been trained, they can be applied directly to new datasets for automated analysis with minimal operator intervention.

Our study presents a novel tool that learns from the expertise of structural geologists and enhances their capabilities while mitigating most sources of subjectivity. The DL-based classifier.

- Processes thousands of images within minutes, dramatically accelerating analysis.
- Eliminates operator dependence, ensuring consistent and reproducible classifications based on a shareable trained network.
- Provides a quantitative measure of classification confidence, enabling geologists to assess how closely a given sample aligns with established fault rock categories.

While our approach enables rapid, automated classification, once a training strategy has been established, it does not replace human expertise. Instead, it serves as an advanced and flexible tool that augments geological interpretation, offering structural geologists an efficient, standardized, and highly scalable method (it can be extended to very large datasets without any significant increase in human effort) for analyzing fault rock microstructures. By integrating deep learning with geological analysis, with quantitative microstructure analysis (morphometry), and with digital rock physics (e.g. direction-dependent permeability simulations), this work marks a step forward in the field, setting a new benchmark for precision and efficiency in fault rock classification.

2. Materials, methods, and geological context

2.1. Approach

Our study is based on three samples collected from the damage zone and fault core of the Trisulti normal fault (Smeraglia et al., 2022a, 2022b) affecting carbonate rocks in the Central Apennine fold-and-thrust belt. The sampled fault rocks exhibit varying degrees of mechanical deformation and are characterized by semi-solid black hydrocarbons (bitumen) occupying rock voids. To investigate their internal structures, samples were analyzed using XRμCT at the Research Center on Nanotechnologies Applied to Engineering (CNIS), Sapienza University of Rome (Italy). The use of XRμCT was crucial because XRμCT provides high-resolution volumetric data in sufficient quantity and quality to support the training phase of a DL tool. Acquiring a comparable dataset using conventional imaging methods, such as optical or electron microscopy, would demand substantially greater effort and cost, particularly due to the need for extensive preparation and analysis of thin sections.

2.2. Geological setting

The fault rock samples are from the Trisulti area in the Central Apennines (Smeraglia et al., 2022a, 2022b; for information on the sampling location and specimens). The Central Apennines represent a fold-and-thrust belt that has evolved since the late Oligocene and continues to be active in its frontal area toward the east. This orogenic system developed in response to the westward subduction of the Adriatic slab beneath the European plate (Carminati et al., 2012). Slab rollback and hinge retreat played a critical role in the tectonic evolution of the region, promoting an eastward migration of compressional deformation (Cavinato and De Celles, 1999).

In the Trisulti area, contractional tectonics deformed the former passive margin of the Adriatic plate, which is predominantly composed of pre- and syn- orogenic Meso-Cenozoic sedimentary successions from the Lazio-Abruzzi paleogeographic domain. These sequences were originally deposited atop the crystalline basement of the Adriatic plate, from which they were subsequently detached. The pre-orogenic deposits consist of Upper Triassic to middle Miocene carbonate platform limestones, while the syn-orogenic sequences, dated from the Miocene to the Pliocene, include marls, siliciclastic sandstones, clays, and conglomerates (Cosentino et al., 2010).

Since the early Miocene, NW–SE-striking thrust faults juxtaposed older carbonate units over younger syn-orogenic sediments, contributing to the structural development of the Central Apennines fold-and-thrust belt. Since the middle to late Miocene, post-orogenic extensional tectonics initiated the formation of NW–SE-striking normal faults. These structures are genetically linked to the opening of the Tyrrhenian back-arc basin and are temporally associated with regional magmatism (Cavinato and De Celles, 1999). Extensional tectonics is still active along the axial region of the Apennines. The geological context of the study area is illustrated in Fig. 1.

2.3. Structural geology context and preparation of the rock samples

The fault rock samples are from the hydrocarbon-stained damage zone and fault core of the Trisulti fault. This structure cuts through Meso-Cenozoic carbonate rocks and offsets a NW–SE-trending anticline composed primarily of Jurassic-Lower Cretaceous limestones (Smeraglia et al., 2022b). The main fault plane strikes NW-SE and dips approximately 80° to the east, displaying extensional kinematics.

The rock microstructures in the different zones are distinct, and the features observed depend on the degree of mechanical deformation, and the observational scale (Fig. 2).

The fault zone records a gradient in deformation intensity, which is expressed through a series of distinct deformation fabrics. The least deformed unit is a *Fractured Limestone*, characterized by pervasive fracturing within a white to light gray limestone matrix. Fractures are typically filled with blackish bitumen, which accentuates the fracture network (Fig. 2a and b and Fig. 3a). The next stage of deformation is represented by a *Breccia*, displaying the result of a more intense deformation, highlighted by presence of bands of fine-grained material. This fabric comprises angular clasts within a poorly sorted, grayish matrix of finer carbonate fragments and bitumen, with less well-defined clast boundaries (Fig. 2c and d and Fig. 3b). The most intensely deformed material is a *Cataclasite*, found closest to the main fault plane. It is composed of variably sized, commonly rounded clasts embedded within a dark gray matrix of fine carbonate particles and bitumen (Fig. 2e and f and Fig. 3c).

The bitumen within the fault rocks enhances the visibility of fractures and fracture relations. In the Fractured Limestone, clasts remain interlocking and fractures are cleanly outlined due to bitumen infill. Virtually no fine-grained material is observed within the fractures, and the bitumen helps to highlight fracture geometry.

In this study, we selected three samples that represent the "ideal" microstructure of each class. These samples were used for both training and validation of the deep learning (DL) network. Additionally, a fourth

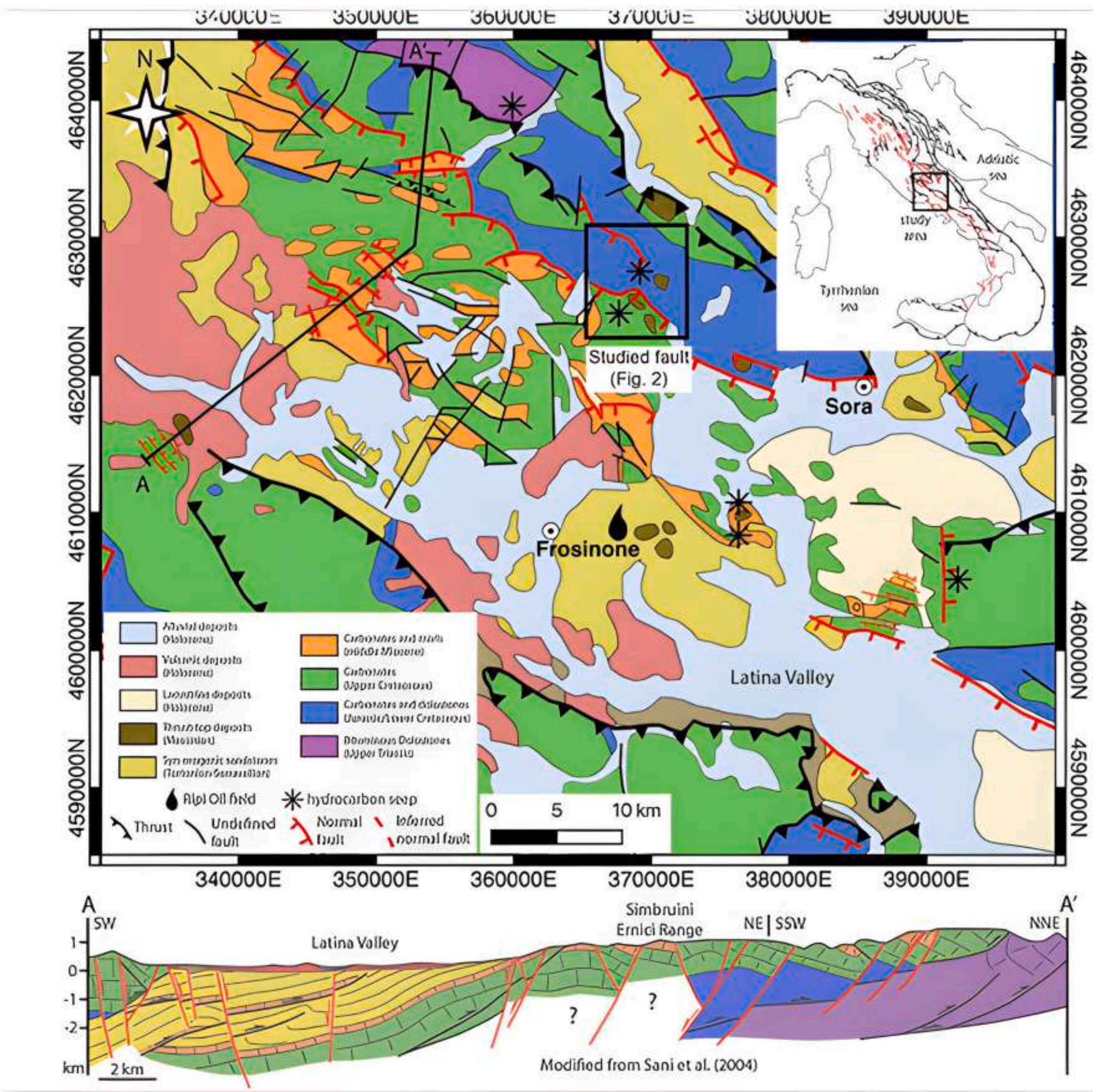

Fig. 1. Geological map and cross section of central Apennines, Italy, showing the geological context in which the samples have been selected. Inset: location of study area in Italy. Box: are with fault shown in Fig. 2.

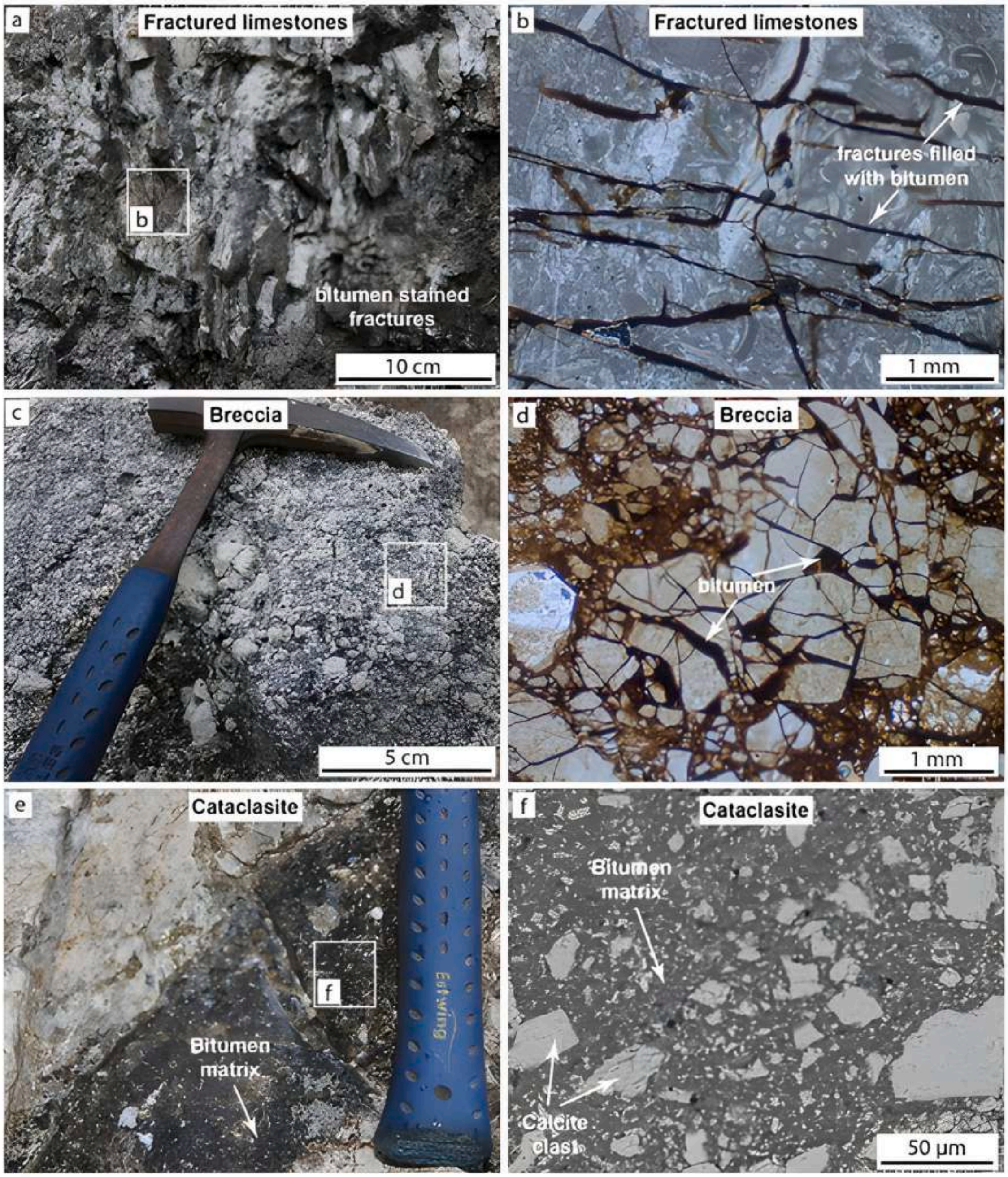

Fig. 2. (a) Fractured limestones in the fault damage zone showing bitumen-filled fractures. (b) Microphotograph under optical microscope of bitumen-filled fractures in the fault damage zone. (c) Bitumen-cemented limestone breccia in the fault damage zone. (d) Microphotograph under optical microscope of bitumen-filled limestone breccia. Notice black to brownish bitumen in the breccia matrix and within clast fractures. The breccia texture varies from crackle to chaotic. (e) Bitumen-cemented limestone cataclasite along the main fault core. (f) Microphotograph under SEM showing the cataclasite matrix characterized by angular limestone clasts scattered within a black bitumen matrix.

sample exhibiting intermediate microstructural characteristics, between Fractured Limestone and Breccia, was chosen to test the DL system on entirely new data. For clarity, and to distinguish it from the three main microstructures while indicating its intermediate degree of deformation, this sample will be referred to as "*FractaBreccia*" throughout this article.

From each microstructural class two samples, prismatic in shape, were cut on a diamond saw. The samples were cut in two different sizes: ~4 cm prisms for low resolution (LD) scans, and ~5 mm pieces for high resolution (HR) scans, as described in the following paragraph.

2.4. X-ray micro-computed tomography data collection

X-ray micro-computed tomography (XRμCT) is a powerful technique for investigating rock microstructures, as it provides non-destructive, high-resolution 3D images that capture both external and internal features. This imaging method can be performed at various resolutions -typically (sub)millimetric, micrometric (Mees et al., 2003; Cnudde et al., 2013), or nanometric (e.g., Nichols et al., 2022)- depending on the combination of X-ray sources, optics, and detectors used. As highlighted in these studies, XRμCT has been widely adopted in geosciences to characterize microstructures and, increasingly, to conduct *in situ* 4D analyses simulating geological processes over time (Voltolini et al.,

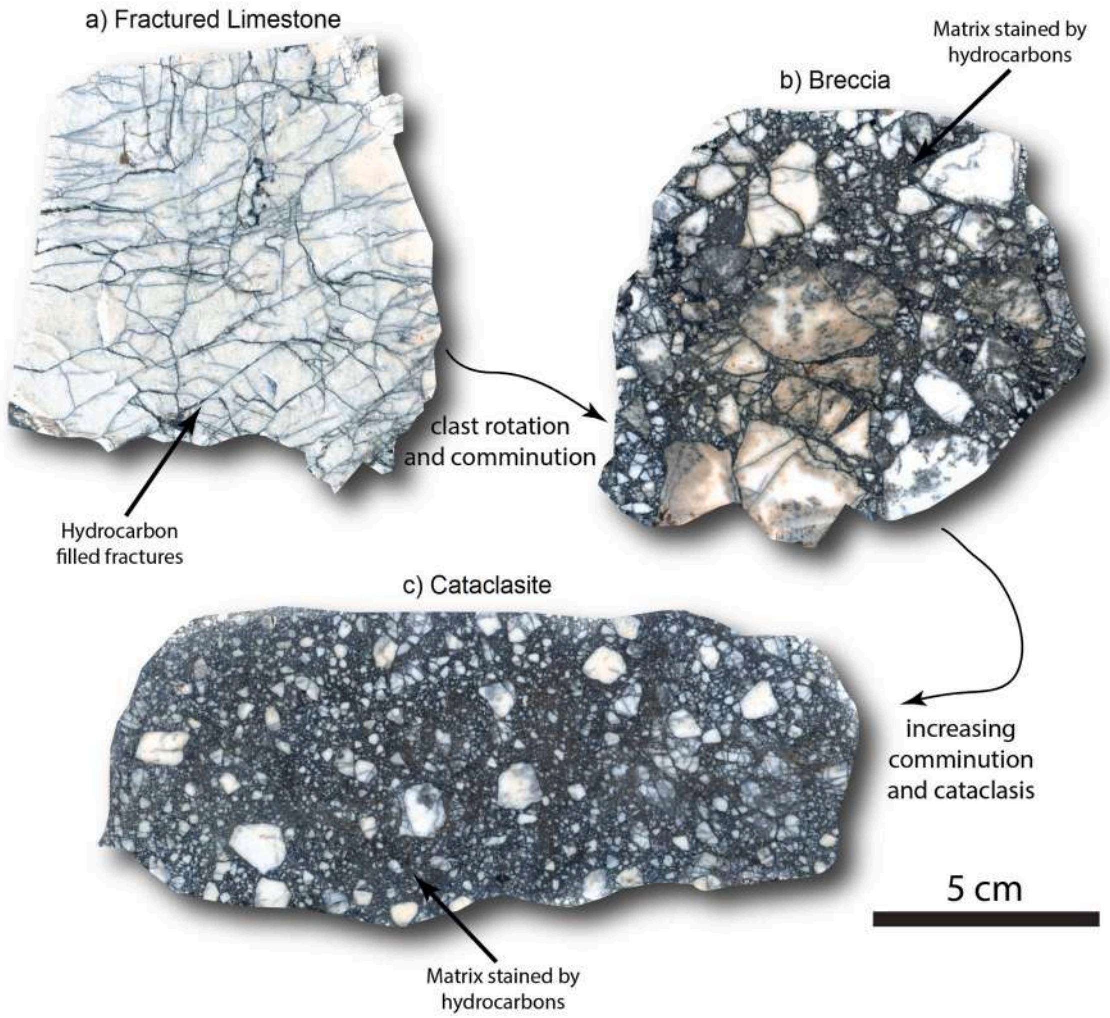

Fig. 3. Photos of the three samples used to define the three classes of microstructures: (a) Fractured limestone; (b) breccia; (c) cataclasite. Notice how the presence of blackish bitumen highlights fractures (dark) and host limestone (light colored, white). Bitumen and matrix content increase from the fractured limestone in the damage zone to the cataclasite in the fault core with increasing clast rotation and comminution due to fault activity. The visual contrast between dark bitumen and pale carbonate rock improves microstructural differentiation which facilitated sample selection and preparation, particularly in cutting and imaging processes.

2017).

In our study, XRμCT was employed at two different resolutions to identify microstructures that vary with scale and to address issues of representativeness. Higher resolution scans allow finer detail to be resolved but at the cost of a smaller field of view (FOV). i.e. volume of the sample, which may result in a sample that is not statistically representative of the whole rock. This representativeness ideally depends both on the specific sample microstructural characteristics (anisotropy, homogeneity, etc.) and the specific morphometric parameter considered. In practice, a trade-off is usually made between resolution and sample volume, or multiple scans at different scales are required to capture the full range of microstructural variability with upscaling and/or hierarchical structures.

Tomographic imaging was performed using a ZEISS Xradia Versa 610 3D X-ray microscope (Carl Zeiss, Oberkochen, Germany). The LR datasets were acquired using the following settings: 0.4 × objective lens, 160 kV voltage, 25 W power, 1 s exposure time, HE2 or HE3 filter, and 1601 projections. HR datasets were obtained using a 4 × objective, 80 kV voltage, 10 W power, 2–4 s exposure time, an LE5 filter, and 2401 projections.

The main parameters and characteristics of the resulting tomographic volumes are summarized in Fig. 4, providing an overview of the sample dimensions and illustrating the effect of scanning the same material at resolutions differing by approximately one order of

	Crackle Breccia HR	Crackle Breccia LR	Breccia HR	Breccia LR	Cataclasite HR	Cataclasite LR
Resolution and FOV						
cube size [vx]	600	300	600	300	600	300
vx size [µm]	3.6	54	3.6	43	3.6	50
cube size [mm^3]	10.1	4251.5	10.1	2146.7	10.1	3375.0
	Fractures-like approach			Fines-like approach		

Fig. 4. Summary of tomographic volume characteristics used in this study. Table colors correspond to different samples and microstructures; title colors denote distinct analytical approaches adopted for the datasets. (For interpretation of the references to color in this figure legend, the reader is referred to the Web version of this article.)

magnitude, in a manner comparable to the multiscale images presented in Fig. 2.

Fig. 5 shows volume renderings of virtual cubes extracted from the HR and LR tomographic datasets for the three sample types used for training. The FractaBreccia sample measurements features are identical to the Fractured Limestone sample. The upper row displays the HR datasets, while the lower row shows their LR counterparts. These renderings illustrate how increasing mechanical deformation intensity in the fault zone has produced distinct microstructures.

In both Figs. 4 and 5, the samples are grouped into two classes that do not carry structural geological meaning but are highly relevant from the perspectives of morphometric analysis and digital rock physics. Samples in the "Fractures-like" class are best analyzed using methods designed for generic fractured media; for example, one can quantify fracture aperture density (morphometry) or simulate the permeability of the fracture network using approaches such as Stokes flow simulation (digital rock physics). This is not the case for samples in the "Fines-like" class, where other properties -such as the relative density of the fines matrix or the orientation of clasts-are more appropriate to evaluate. The implications of this analysis-oriented classification will be explored in detail in a future study through a comprehensive set of examples. Nevertheless, it is important to mention it briefly here, as the DL system not only identified microstructures quantitatively but also indicated the most suitable analytical approach for characterizing each microstructure in these limestone samples.

2.5. Development of the deep learning-based classifier

The purpose of our classification tool is twofold: 1) to obtain a fast and fully quantitative classification system for limestone fault rocks. 2) Use the classification results to guide the morphometric and digital rock physics analyses to run on the samples. In this sense the quantitative classification is not necessary only for a descriptive standpoint, but also as a guide for the possible analyses to run on the specific datasets. Following XRμCT data collection, it became evident that a unified analytical approach applicable to all samples and resolutions was not feasible. Distinct microstructural types necessitated tailored methodologies. Our analysis identified two primary strategies.

1. A "fractured-like" approach, treating the sample as a solid with discrete fractures.
2. A "fines-like" approach, representing the sample as clasts dispersed in a fine-grained matrix.

We define as "matrix" the material composed of fragments unresolved at the given resolution. The fractured-like class supports measurements such as fracture orientation, aperture size distribution, and permeability, whereas the Fines-like class allows the analysis of clast shape orientation, a metric that is irrelevant in predominantly fractured materials. Sample evaluation from a morphometric analysis point of view suggested that the fractured-like approach is best suited for the Fractured Limestone (HR and LR) and Breccia HR datasets, while the fines-like method is more appropriate for Breccia LR and both resolutions of the Cataclasite samples (see color coding in Fig. 4, top row).

For the Breccia sample the morphometric analysis classification depends on image resolution. At HR, the breccia has a fractured-like texture; at LR, finer features are below resolution, and the resulting volume appears to be matrix-supported. This is because in XRμCT, voxel size constrains the minimum resolvable feature. For example, a voxel measuring 10 μm partially filled with calcite and air will yield a grayscale value between those of pure phases. This averaging, termed partial volume effect, is most pronounced in the fines, where carbonate rock, bitumen, and voids are intermixed.

Grayscale intensity in the XRμCT images reflects X-ray attenuation:

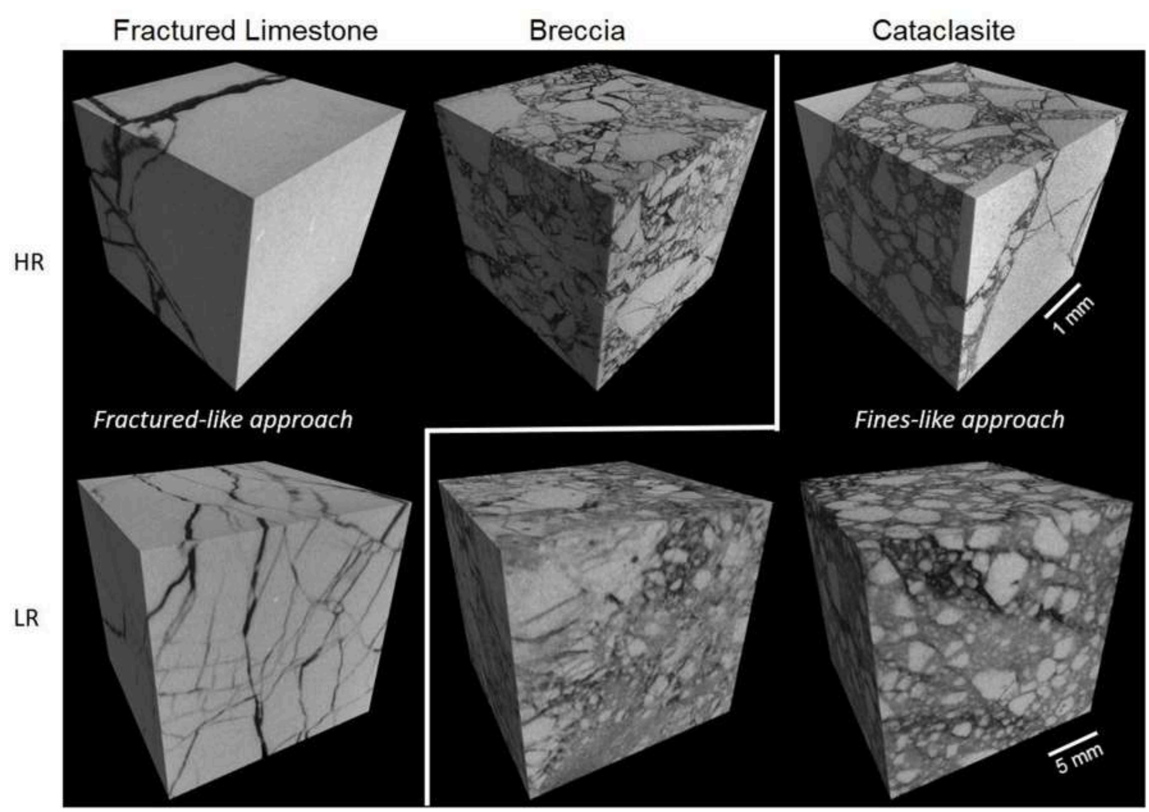

Fig. 5. Volume renderings of samples from the three fault rock classes. For the size of the different cubes, refer to the table in Fig. 4. Samples are divided by microstructure type (Fractured Limestone, Breccia, and Cataclasite), resolution (high resolution HR, and low resolution LR), and suggested analytical approach (Fractured- and Fines-like).

carbonates appear light gray, voids (air) appear nearly black, bitumen is markedly darker gray than carbonates, and fines occupy intermediate shades depending on composition (and therefore X-ray attenuation). This grayscale spatial distribution forms the basis of our deep learning classifier.

Although a simple binary classification (fractured-like vs. fines-like) might suffice for morphometric analysis purposes, we opted for a more granular classification based on geologically meaningful rock fabric, focusing on building fully quantitative classification capabilities for fault rocks in the area: Fractured Limestone, Breccia, and Cataclasite. This approach enhances the versatility of the classifier and ensures compatibility with subsequent analysis procedures. For example, as shown in Fig. 6, fluid flow simulations (e.g., Stokes flow modeling) can be meaningfully applied to Fractured Limestone, while orientation analysis of clasts (e.g., for detecting shear-related fabrics) is better suited to Cataclasite. This figure is only displayed to offer to the reader an example of the potential analyses on the different classes of samples, but this analysis part will the focus of a different work, and mentioned here only to give an example of the guidance that this classification can provide (see Fig. 7).

To develop this machine learning-assisted classifier, we used MATLAB's Deep Learning Toolbox (MATLAB® Version 9.13.0.2126072 (R2022b), Deep Learning Toolbox Version 14.5). We adopted a 2D classification approach to maximize data availability and model flexibility. A 3D classifier would require an impractical number of tomographic scans (hundreds at least) and significantly more computational resources not available on a standard workstation. In contrast, the 2D method allows efficient training and analysis, and -notably- can be extended to other imaging techniques, such as scanning electron microscopy (SEM) or optical microscopy, provided they yield grayscale images with comparable resolution and contrast to XRμCT. We presented an example of this extended capabilities in our work.

Using 2D tomographic slices also enables volume-wise classification, where slices along the scanning direction can highlight microstructural inhomogeneities and improve statistical robustness. Moreover, 2D methods facilitate automated high-throughput data generation, including from photomicrographs or SEM images, making them well-suited for constructing large training datasets.

The process begins by slicing the 3D XRμCT volumes into 2D TIFF images. Low-resolution (LR) datasets, sized 300^3 voxels, yield 300 images at 300 × 300 pixels when sliced in a single direction. High-resolution (HR) datasets, sized 600^3 voxels, yield 600 images at 600 × 600 pixels. Slicing along the two orthogonal planes adds 600 images for LR and 1200 for HR. To further expand the dataset, each image can be randomly rotated within a ±180° range during training. This strategy allows rapid and efficient generation of large, diverse 2D datasets from a limited number of 3D scans.

Among the various network architectures available in MATLAB, we selected GoogLeNet due to its robust performance in image classification tasks across disciplines (Singla et al., 2016; Yilmaz and Trocan, 2021; Yuesheng et al., 2021). GoogLeNet is a 22-layer deep convolutional neural network based on inception modules (Szegedy et al., 2015), offering strong performance with relatively low computational demand—making it suitable for training and deployment on standard desktop machines.

The model was adapted to classify each input image into one of three predefined fault rock classes: Fractured Limestone, Breccia, or Cataclasite. Each classification result is also associated with a set of probability scores reflecting the degree of membership in each class. The resulting tool is designed to operate independently of user interpretation and can classify any image consistent with the type and resolution of the training data.

Once the neural network architecture was selected and tailored to meet our input-output requirements, the next step was to choose the training set. Given the different image sizes, the two magnifications were processed using separate networks specific to each resolution. Each tomographic volume was sliced, as described previously, to obtain 2D images for training. The high-resolution (HR) dataset used 400 randomly selected images per class (with added random rotations), while the low-resolution (LR) dataset used 300 images per class. Each dataset underwent 312 iterations across 4 epochs, resulting in an evaluated accuracy of approximately 100 % and a loss function very close to

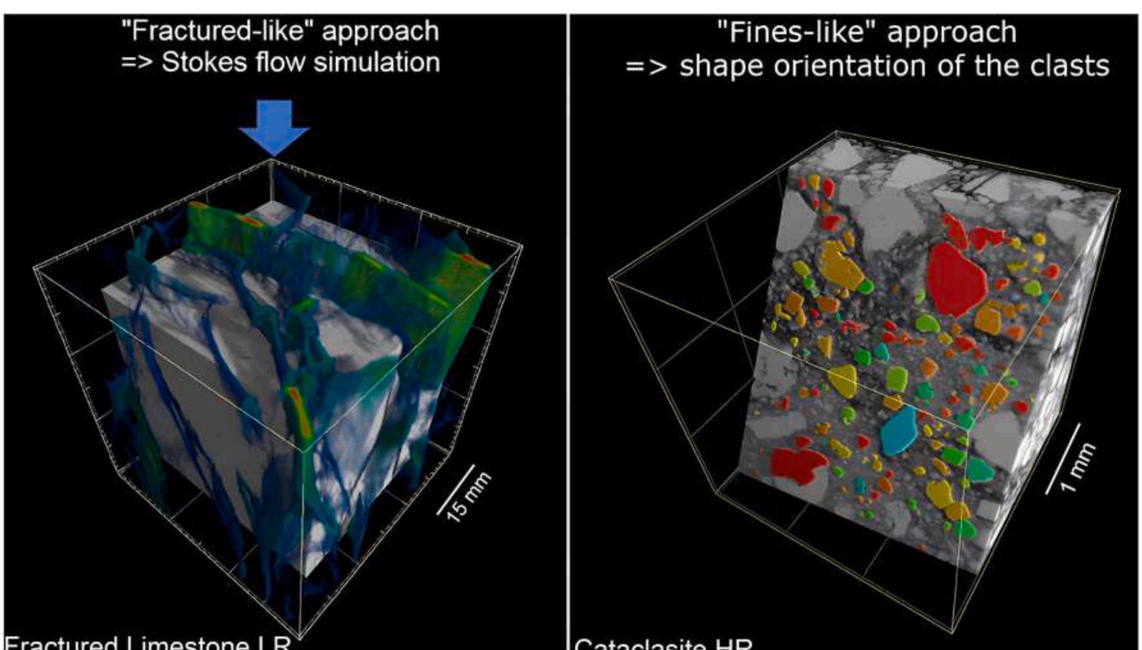

Fig. 6. Two examples of how classification guides specific analyses of fault rock microstructures: in a Fractured Limestone (LR), Stokes flow simulations enable estimation of permeability and identification of preferential flow paths; in a Cataclasite (HR), clast orientation analysis reveals potential shear fabrics (orientation color-coded). The Fractured Limestone LR cube has a side length of 16.20 mm, whereas the Cataclasite HR cube measures 2.16 mm per side. (For interpretation of the references to color in this figure legend, the reader is referred to the Web version of this article.)

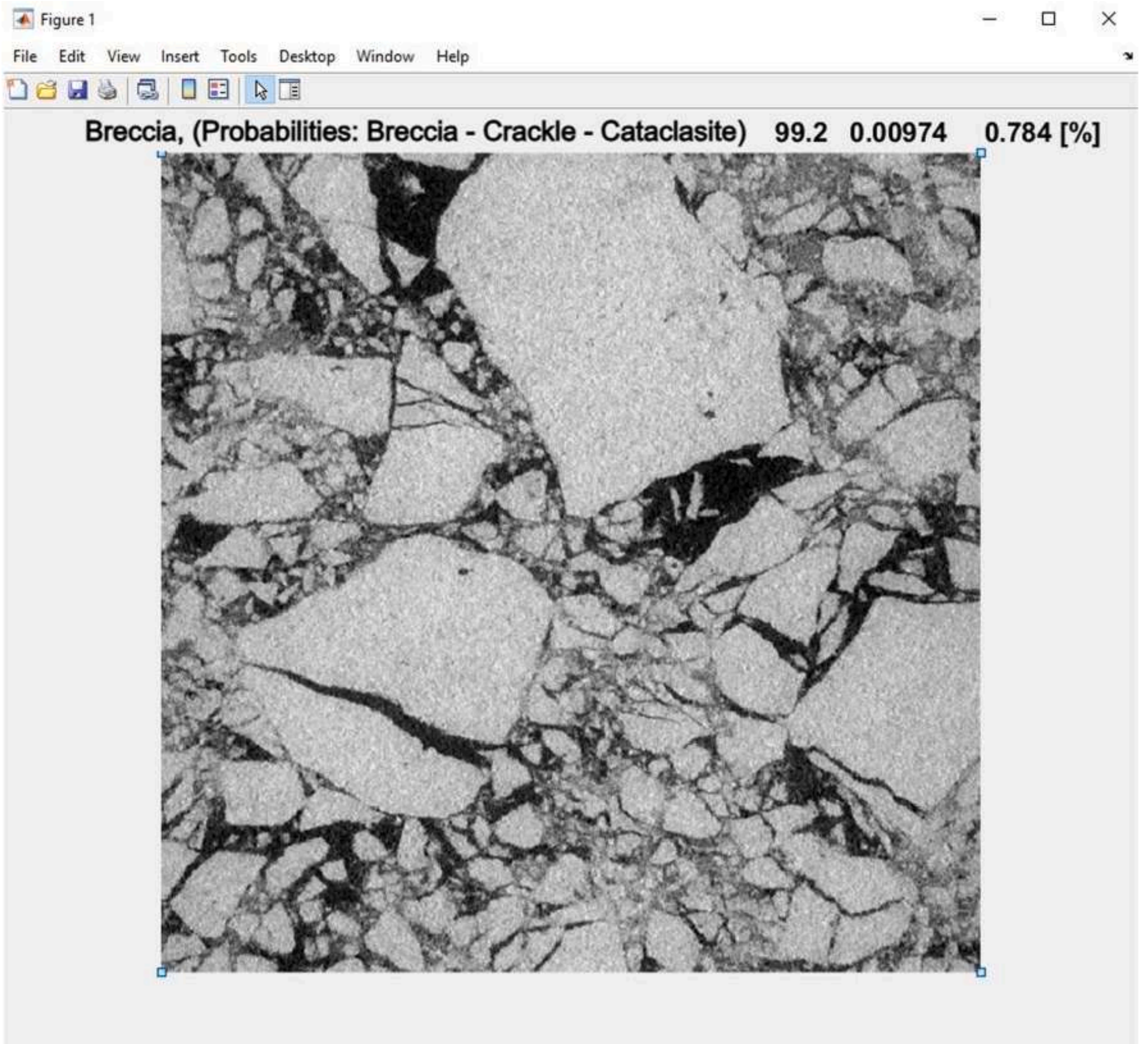

Fig. 7. Example of a simple classification of a single image: a Breccia HR sample was evaluated, and the probability values for belonging to each of the three classes are displayed. The tool identified the sample as Breccia with a 99.2 % probability. Image size = 2.16 mm × 2.16 mm.

0. The training process, depending on the chosen parameters, took between a few minutes and up to 100 min on a standard computer.

Following training, the network was exported to the MATLAB environment and can be used to classify new images. A basic evaluator script was developed for classifying individual images, while more comprehensive scripts capable of handling thousands of images -offering live updates, automated result saving, and plotting-were also created, as detailed later.

Testing on the training datasets, including new slices cut from different orientations, produced high classification accuracy (see Results). After validating the basic script, we incorporated it into a full classification workflow including the plotting into a ternary diagram.

The need for a DL-based approach to fault rock classification, compared with current state-of-the-art methods, can be summarized as follows. 1) *Visual inspection*: relying solely on an operator's personal expertise to classify images presents several disadvantages: consistency (operator-dependent) of the analysis, speed, qualitative results (or semi-quantitative at best). 2) *Morphometric analysis*: the operator input (and therefore potential biases) is still important (e.g. choice of the segmentation strategy, filtering, choice of the morphometric parameters, etc.), it is substantially slower than ML-based approaches and less automatable and more prone to issues due to varying image quality. ML-based approaches are also the advantage of being of learning complex, high-dimensional patterns (compared to the 2D info of morphometry on images) beyond human-defined metrics.

ML-based methods have the disadvantages of requiring a large amount of data for training, already classified in the case of supervised networks (as the one proposed in this work), and the classification strategy is more obscure to the user compared to morphometric analysis where parameters with a clear physical meaning are measured (object roundness, area, connectivity, aspect ratio, etc.). An illustrative comparison of these approaches is provided by Azimi et al. (2018), who compared microstructure classification using deep learning and morphometric methods. It is worth noting that deep learning has advanced considerably since 2018, further widening the gap between the two approaches. Some more helpful information can be found in Wang et al. (2024) about the classification of sandstones.

Testing on the training datasets, including new slices cut from different directions, produced very satisfactory results in terms of classification accuracy (further details are provided in the Results section). Once the basic classification script was validated, the process was incorporated into a more comprehensive classification workflow.

One of the key advantages of the ML-based classification approach is that the neural network assigns a probability to each microstructure class on each image. These probabilities can be used to estimate the relative abundance of each microstructure within an image, enabling a fully quantitative classification.

To leverage this capability, a ternary diagram for limestone fault rocks was developed, with the vertices representing the three classes from the training datasets: fractured limestone with Fractured Limestone texture, Breccia, and Cataclasite. Any new image can then be classified and plotted on this diagram to assess its characteristics. A script has been developed to handle bulk classification, evaluating hundreds of images and plotting the results in the ternary diagram. A notable advantage of using neural networks over human classification is speed: this tool can evaluate 400 images and generate the final ternary plot in just 45 s, including live updates for monitoring purposes.

3. Results and discussion

The first step in the analysis is to look for the validation of the approach. Validation was conducted using slices from the training datasets. The goal was to confirm that the classification probabilities for each sample would closely approach 100 % for the respective class. For the LR datasets, 100 randomly chosen images from each class were evaluated, yielding the following average classification probabilities: Fractured Limestone = 99.94 %, Breccia = 99.63 %, and Cataclasite = 99.94 %. As shown in the ternary diagram in Fig. 8, the data points are tightly clustered near the vertices. Each dataset is color-coded, and despite the 100 data points per dataset, it is visually impossible to distinguish them because of the tight clustering.

The only class showing slight variability is Breccia, where a few images exhibit minimal characteristics of Cataclasite, indicating a slight "cataclasite-ness" in the LR dataset in a few images. However, these exceptions are negligible, and the overall classification accuracy remains exceptionally high. In the HR datasets the clustering of the three classes is virtually perfect.

To add additional information to the classification results, about the position in the sample of the analyzed image, when working with volumes cut as single image stacks, the software incorporates a color-coding system: data points are assigned specific color hues, with brightness varying based on the image's position in the series of images (assuming the series of images chosen is a full stack of tomographic slices following a specific direction). This feature is particularly useful when working with tomographic datasets, especially when evaluating a stack of 2D slices (typically the slices cut normal to the vertical direction, the rotation axis during the measurement. Tomographic datasets are often saved in this fashion). The brightness of the data points indicates the relative position of the slice in the stack, where brighter points (of a given color) correspond to slices closer to the top of the stack.

When working with HR datasets, the situation improves further due to the higher resolution (measured by the number of pixels per image, not the magnification of the measurement). With higher resolution images, the neural network is able to distinguish between classes with even greater accuracy, achieving a classification probability of 100 % for each class.

While the validation using training samples, even when resliced, is expected to produce excellent results, a more meaningful test was conducted using a new XRμCT scan of a fresh sample. This sample, named "*FractaBreccia*" for identification purposes was collected from the damage zone between Fractured Limestone and Breccia samples. This sample was a very suitable candidate for evaluating the performance of the deep learning tool. Qualitatively, the sample appears to be a Fractured Limestone with a higher density of fractures and some areas showing more pervasive mechanical alteration, with the presence of fine-grained material. Therefore, we expected the sample to classify as Fractured Limestone.

The LR dataset, consisting of 300 evaluated images, identified the sample as follows: 96.40 % Fractured Limestone, 3.04 % Breccia, and 0.56 % Cataclasite. The classification places it as expected within the Fractured Limestone category. However, interesting features emerge when examining the ternary diagram. While most data points are clustered near the Fractured Limestone vertex, a noticeable spread towards the Breccia vertex suggests some variability in the "breccia-ness" character of the FractaBreccia.

This sample highlights an important feature that was not observable with the validation datasets: if microstructural heterogeneity is present, in the stacking direction, the classification system can highlight it and visualize the spread of the classification parameters on the ternary diagram. In addition to the spread, the color can provide the information about each specific point about their position in the stack (i.e. if closer to the top -brighter color- or to the bottom), in case of tomographic datasets with a single slicing direction.

The mechanical damage in limestone, from the outer zone going towards the fault core, is expected to follow the sequence: Fractured Limestone → Breccia → Cataclasite. In a ternary diagram, this progression would ideally trace a path along two sides of the triangle. Consistent with this general trend, our samples are located within this region of the ternary diagram.

The FractaBreccia sample displays a heterogeneity-dependent behavior, as highlighted from the classification spread of the LR dataset. The higher magnification image has a narrow the field of view, and captures an area where the Fractured Limestone microstructure predominates. Visual inspection reveals no difference between the high-resolution samples, and the software also identifies the sample as Fractured Limestone with an average classification probability of 99.98

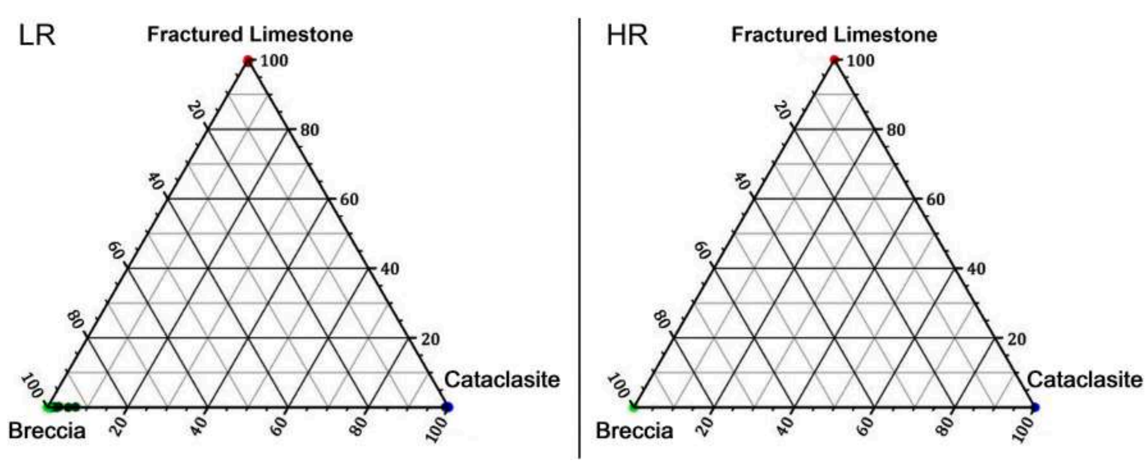

Fig. 8. Ternary diagram of the training samples used for validation, after reslicing the volumes. The classification of LR samples is nearly flawless, with datasets color-coded as follows: red for Fractured Limestone, green for Breccia, and blue for Cataclasite. Hue intensity refers to the position of the specific image in the stack. In the HR samples, the three datasets, each consisting of 100 data points, perfectly align with their respective vertices. (For interpretation of the references to color in this figure legend, the reader is referred to the Web version of this article.)

% based on 600 images. These results highlight the importance of multi-scale measurements: not only some microstructural features can be only visualized at specific resolutions, but also heterogeneity issues can be identified, when present. Unfortunately, the upscaling problems in imaging are bound by the hard relationship resolution vs. field of view, i.e. only a small volume of a sample can be measured at high resolution, and a large volume would require a low resolution measurement.

The analysis of the sample FractaBreccia LR reveals how this classification tool is helpful in identifying heterogeneities in a volume. In Fig. 9 (left) the points (i.e. the images in the stack obtained from the volume) display a spread, with points concentrated close to the "Fractured Limestone" class vertex, but with a number of points going towards the Breccia class vertex. The meaning of these points is that there are images where the microstructure is like a Fractured Limestone, but with a component of the microstructure of the Breccia class. The intensity of color (magenta) also gives the information about the position in the stack of those images. Specifically, since the points farthest from the Fractured Limestone vertex are light magenta, this means that the images with a more Breccia component in their microstructure are close to the top of the sample. Fig. 10 display this specific feature: for FractaBreccia LR two different images are shown. The image on the left represent a microstructure very close to a perfect Fractured Limestone, while the image on the right display a 68 % Fractured Limestone component. By visual inspection it is easy to see how the image on the left is virtually undistinguishable from the Fractured Limestone sample used for training. On the other hand, the image on the right displays a more convoluted fracture system geometry, with the presence of a small amount of fine-grained material which is not present in the Fractured Limestone microstructure, but it is present in the Breccia. This classification system, once trained, enables such analyses to be performed in just a few minutes per sample.

This approach can be extended and tested with various imaging datasets. While the primary focus of this work is the classification of fault rocks from the Trisulti fault zone, intended to support subsequent morphometric analysis and modeling of their anisotropic properties, the method's flexibility is also of great interest for a broader audience and utilization. The training datasets used here are specific, meaning that the generalization of the trained network to samples with different lithologies or imaging techniques is not expected to yield equally accurate results.

To check how this approach can be generalizable we tested our already trained neural network (using XRμCT data) on three images from Billi (2010), which depict highly damaged carbonate rocks from a fault area near Monte Maggiore (Caserta, Italy). These images, obtained through optical microscopy, were inverted and converted to grayscale to mimic the features of XRμCT data, where opacity correlates with brightness. This demonstrates that, despite the imaging method shift from X-ray attenuation to visible light attenuation as the imaging technique, the microstructural features are still compatible and represent similar structures. These images are ideal from a microstructural point of view, since thay have been collected on similar mechanically altered limestones. From the imaging point of view, optical microscopy gives different results, in terms of mapping the microstructure, hence the need of applying software filters to convert the thin section images to images where fractures are dark and calcium carbonate is light, in a graysacale lookup table. For this specific samples, rescaling to the same pixel size of the XRμCT data, an 8-bit grayscale conversion followed by a lookup table inversion was the only preprocessing needed, on photographs taken with parallel polars (transmitted light). Other imaging techniques can be considered, especially scanning electron microscopy backscattering (SEM/BSE) images since the grayscale of the different phases in the sample typically correspond very well to what it is seen in XRμCT data (from a practical purpose, the Z-dependence of the graylevels contrast in SEM/BSE is very similar to the XR linear attenuation coefficients-related signal mapped by XRμCT, therefore a very high data compatibility is expected).

Billi's (2010) study is especially valuable in our context because it categorizes a cataclasite into three evolution stages: embryonic, intermediate, and mature. Since the rock in question is a limestone with a very similar microstructure and deformation history. The embryonic cataclasite looks intermediate between Fractured Limestone and Breccia; the intermediate cataclasite resembles the brecciated sample with more fines; and the mature cataclasite is nearly identical to our Cataclasite sample, with rounded clasts embedded in a fine matrix of varying density.

When classified by the neural network, the points in the ternary diagram align with these qualitative observations, providing a quantitative characterization of the fabric evolution (Fig. 11).

The expected fabric path depending on the degree of mechanical alteration in function of the position of the sample with respect to the fault core is highlighted by the arrow shown in Fig. 11, following the Fractured Limestone → Breccia → Cataclasite path (moving from the outer zone towards the fault core). While with tomographic data only the end members and a sample (that for ease of classification we called FractaBreccia) between the Fractured Limestone and the Breccia classes were available, the data recovered from literature with fabrics more in the Breccia – Cataclasite path were extremely valuable to test the DL classification system. All the images we have used for training and classification follow this path, with the new images being distributed between Breccia and Cataclasite depending on the extent of mechanical alteration, as highlighted by the original article where these samples were labeled as "Embryonic Cataclsite", "Intermediate Cataclasite", and "Mature Cataclasite", in order of increasing mechanical deformation. In our classification system, the Embryonic Cataclasite is close to the

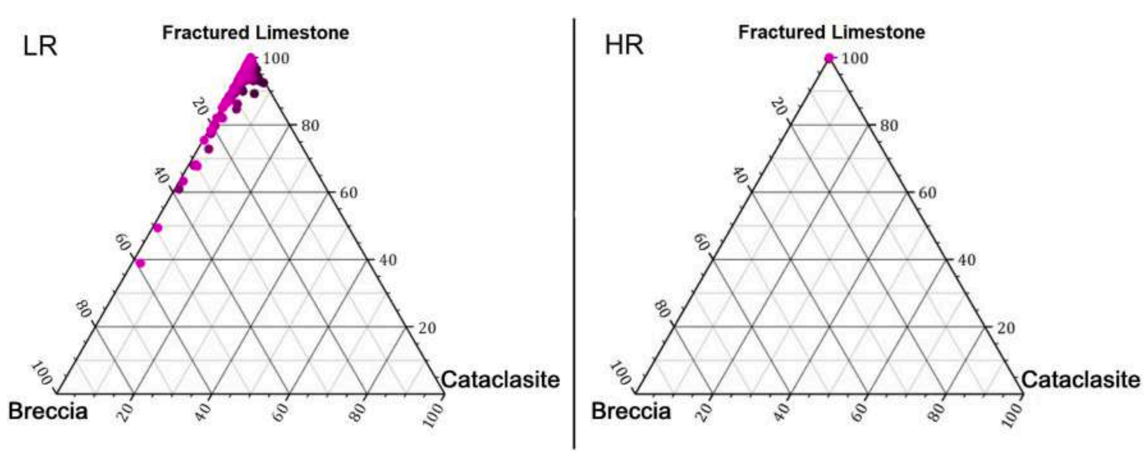

Fig. 9. Ternary diagram plotting the identification probabilities of the images obtained from the FractaBreccia sample, both LR (300 images) and HR (600 images).

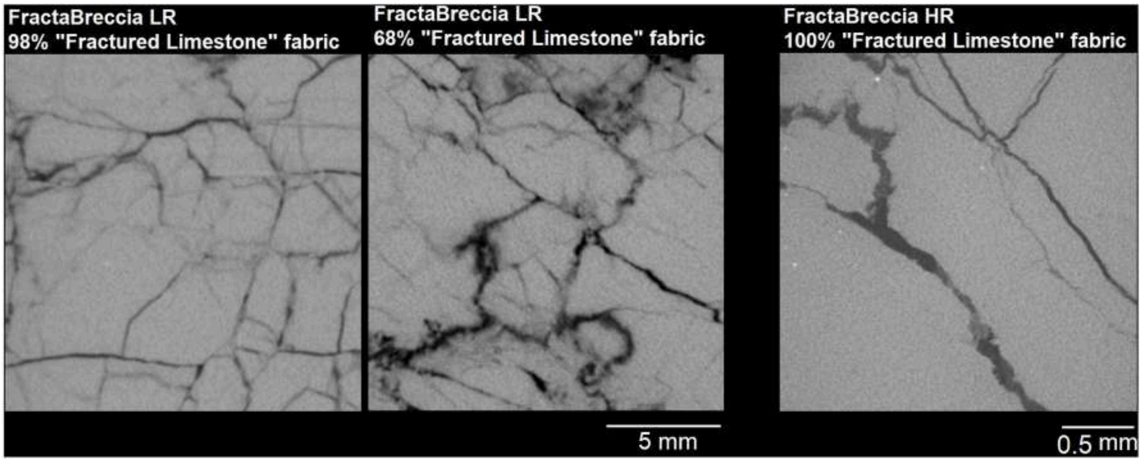

Fig. 10. Examples of images from the classification run summarized in Fig. 9. The HR dataset looks like a Fractured Limestone, while the LR dataset resulted in a classification as a Fractured Limestone with different degrees of breccia-ness, depending on the position in the sample. Image size of LR image = 15 mm × 15 mm; HR image = 2.16 mm × 2.16 mm.

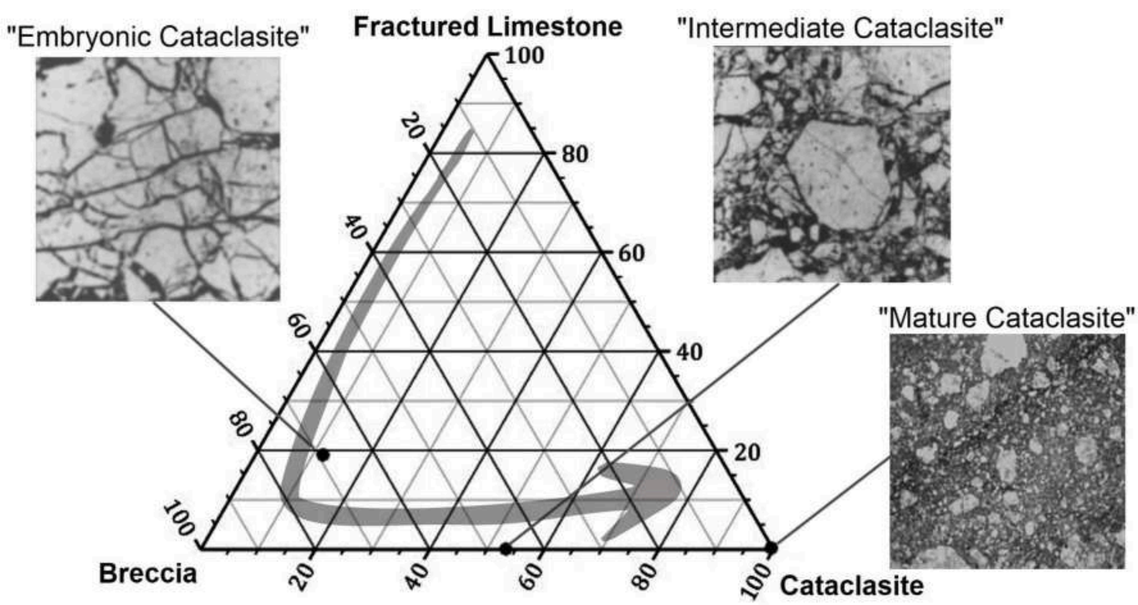

Fig. 11. Ternary diagram showing the classification probabilities of images from Billi (2010). The optical microscopy images were converted to a format compatible with the classification software. The arrow marks the ideal path of a limestone with increasing mechanical deformation in the context of the ternary diagram. Images Field of view of sample images = 5 mm × 5 mm.

Breccia vertex, but still with a significant amount of microstructural characteristics of Fractured Limestone and Cataclasite. The Intermediate Cataclasite sample falls almost perfectly in between the Breccia and Cataclasite classes. Lastly the Cataclasite from Billi (2010) corresponds to the Cataclasite microstructure used for training the neural network. These results are very encouraging, since they suggest that the classification system can work with different image sources, if the microstructure can be made compatible from a grayscale point of view. On the other hand, these samples are extremely similar in lithology to the ones used in our training network, therefore positive results are expected. How well this approach would work with different lithologies is debatable, but we expect it not to work with rock having specific intrinsic microstructure different from a microcrystalline limestone (e.g. a granite). In any case, for any family of rocks a specific training would be advised for best accuracy of the results. This means it is required to find three samples describing the ideal structures to use as end member (hence the importance of the human contribution in the training phase), and subsequently classify all the other samples using that specific trained network.

This example also underscores a key limitation of our classification approach: the quality of a supervised machine learning (ML) model is directly dependent on the selection and quantity of training datasets. The classification can only be as accurate as the training process is. Acquiring large volumes of well-defined image data for each class is a significant challenge. In the case of optical and electron microscopy, generating hundreds of images for each dataset becomes cumbersome, especially without automated data acquisition systems, as an expert must first evaluate each image to ensure it belongs to the correct class. In contrast, XRμCT offers a practical advantage, as a single measurement can yield hundreds or even thousands of images of a sample through volume slicing.

Another compelling feature of this approach is its ability to classify samples in a user-independent manner once the training phase is complete. This is valuable because it eliminates user bias, making the classification process more objective. Moreover, the trained network. mat files can be easily shared with other researchers, allowing them to use the same procedure to classify their own samples. This flexibility is especially striking in the final test: images collected by different researchers, from various fault rock samples (similar in lithology and deformation processes), can be classified successfully without the need to build a new training dataset specific to optical microscopy or other imaging techniques.

4. Conclusions

This work introduces a novel machine learning-based approach for the classification of fault rocks in carbonates, leveraging deep learning's proven capabilities in image recognition and classification. Deep learning neural networks have demonstrated exceptional performance across various fields, and this study highlights how these capabilities can be effectively applied to fault rock fabric classification. By utilizing a Matlab toolbox and XRμCT datasets for neural network training, this method is accessible even to non-specialists, making it a highly compelling tool for fault rock analysis.

In the field of machine learning, there is often a tendency to develop systems aimed at replacing human expertise. For example, some image processing techniques attempt to entirely substitute human image analysts. While this goal is understandable, it overlooks a critical point: expert input remains indispensable, particularly during the training phase. The quality of the classification results is directly tied to the careful selection of the training datasets, which requires expert knowledge to ensure meaningful and accurate outcomes. Even in unsupervised learning systems, expert evaluation is crucial for validating the results and providing scientific context. In the case of fault rocks, structural geologists are essential for interpreting the classification results, especially in terms of understanding the degree of damage, and especially its implication in the wider context. The collaboration of experts in structural geology, image processing, and modeling is necessary for meaningful analysis.

The results presented here demonstrate that this machine learning tool is a powerful and flexible asset for classifying rock fabrics. Its ability to process diverse types of data -such as the test conducted with optical microscopy images-illustrates its broad applicability. However, one of the key limitations of this approach is the need for properly labeled datasets, which are essential for training supervised learning models. The quality and quantity of data are paramount for building a robust training set. Fortunately, XRμCT data proves to be a proper source for generating large, high-quality datasets needed for this task.

Ultimately, our work shows that a machine learning-based classification system, trained on XRμCT data, is a highly effective tool for quantitatively analyzing carbonate fault rock fabrics. It provides a solid foundation for further morphometric analyses and modeling of the anisotropic properties of fault rocks, contributing to a more comprehensive understanding of their mechanical and structural characteristics.

CRediT authorship contribution statement

Marco Voltolini: Writing – review & editing, Writing – original draft, Visualization, Software, Methodology, Investigation, Formal analysis, Conceptualization. **Luca Smeraglia:** Writing – review & editing, Writing – original draft, Visualization, Resources, Investigation, Conceptualization. **Andrea Billi:** Writing – review & editing, Writing – original draft, Visualization, Resources, Investigation, Conceptualization. **Eugenio Carminati:** Writing – review & editing, Writing – original draft, Validation, Resources, Investigation, Conceptualization. **Flavio Cognigni:** Writing – original draft, Methodology, Investigation. **Marco Rossi:** Investigation. **Michele Zucali:** Resources, Investigation, Conceptualization.

Declaration of competing interest

The authors declare that they have no known competing financial interests or personal relationships that could have appeared to influence the work reported in this paper.

Acknowledgements

The authors acknowledge two anonymous reviewers that helped to substantially improve the manuscript.

Data availability

Data will be made available on request.

References

Ahr, W.M., 2011. Geology of Carbonate Reservoirs: the Identification, Description and Characterization of Hydrocarbon Reservoirs in Carbonate Rocks. John Wiley & Sons.
Ak, A., Topuz, V., Midi, I., 2022. Motor imagery EEG signal classification using image processing technique over GoogLeNet deep learning algorithm for controlling the robot manipulator. Biomed. Signal Process Control 72, 103295.
Al-Huseiny, M.S., Sajit, A.S., 2021. Transfer learning with GoogLeNet for detection of lung cancer. Indonesian Journal of Electrical Engineering and computer science 22 (2), 1078–1086.
Andrews, B.J., Roberts, J.J., Shipton, Z.K., Bigi, S., Tartarello, M.C., Johnson, G., 2019. How do we see fractures? Quantifying subjective bias in fracture data collection. Solid Earth 10 (2), 487–516.
Annunziatellis, A., Beaubien, S.E., Bigi, S., Ciotoli, G., Coltella, M., Lombardi, S., 2008. Gas migration along fault systems and through the vadose zone in the Latera caldera (central Italy): implications for CO2 geological storage. Int. J. Greenh. Gas Control 2 (3), 353–372.
Azimi, S.M., Britz, D., Engstler, M., Fritz, M., Mücklich, F., 2018. Advanced steel microstructural classification by deep learning methods. Sci. Rep. 8 (1), 2128.
Billi, Andrea, 2010. Microtectonics of low-P low-T carbonate fault rocks. J. Struct. Geol. 32 (9), 1392–1402.
Burchette, T.P., 2012. Carbonate rocks and petroleum reservoirs: a geological perspective from the industry. Geological Society, London, Special Publications 370 (1), 17–37.
Caine, J.S., Evans, J.P., Forster, C.B., 1996. Fault zone architecture and permeability structure. Geology 24, 1025–1028.
Carminati, E., Lustrino, M., Doglioni, C., 2012. Geodynamic evolution of the central and western mediterranean: tectonics vs. igneous petrology constraints. Tectonophysics 579, 173–192.
Cavinato, G.P., Celles, P.D., 1999. Extensional basins in the tectonically bimodal central Apennines fold-thrust belt, Italy: response to corner flow above a subducting slab in retrograde motion. Geology 27 (10), 955–958.
Cosentino, D., Cipollari, P., Marsili, P., Scrocca, D., 2010. Geology of the central apennines: a regional review. Journal of the virtual explorer 36 (11), 1–37.
dos Anjos, C.E., Avila, M.R., Vasconcelos, A.G., Pereira Neta, A.M., Medeiros, L.C., Evsukoff, A.G., Surmas, R., Landau, L., 2021. Deep learning for lithological classification of carbonate rock micro-CT images. Comput. Geosci. 25, 971–983.
Evans, J.P., Forster, C.B., Goddard, J.V., 1997. Permeability of fault-related rocks, and implications for hydraulic structure of fault zones. J. Struct. Geol. 19 (11), 1393–1404.
Jordan, M.I., Mitchell, T.M., 2015. Machine learning: trends, perspectives, and prospects. Science 349 (6245), 255–260.
Knaup, A., Jernigen, J., Curtis, M., Devegowda, D., Sondergeld, C., Rai, C., 2022. Application of deep learning to shale microstructure classification. Mar. Petrol. Geol. 144, 105842.
Lan, Q., Xu, M., Binazadeh, M., Dehghanpour, H., Wood, J.M., 2015. A comparative investigation of shale wettability: the significance of pore connectivity. J. Nat. Gas Sci. Eng. 27, 1174–1188.
Lucia, F.J., Kerans, C., Jennings Jr, J.W., 2003. Carbonate reservoir characterization. Journal of petroleum technology 55 (6), 70–72.
Lyons, M., 2021. Ceramic fabric classification of petrographic thin sections with deep learning. Journal of Computer Applications in Archaeology 4 (1).
Maclay, R.W., Small, T.A., 1984. Carbonate Geology and Hydrology of the Edwards Aquifer in the San Antonio Area. US Geological Survey, Texas. No. 83-537.
Mees, F., Swennen, R., Geet, M.V., Jacobs, P., 2003. Applications of X-ray computed tomography in the geosciences. Geological Society 215 (1), 1–6. London, Special Publications.
Mort, K., Woodcock, N.H., 2008. Quantifying fault breccia geometry: dent fault, NW England. J. Struct. Geol. 30 (6), 701–709.
Mudry, J., Charmoille, A., Robbe, N., Bertrand, C., Batiot, C., Emblanch, C., Mettetal, J. P., 2002. Use of hydrogeochemistry to display a present recharge of confined karst aquifers: case study of the Doubs valley, Jura mountains, eastern France. Karst and Environment 123–129.
Młynarczuk, M., Górszczyk, A., Ślipek, B., 2013. The application of pattern recognition in the automatic classification of microscopic rock images. Comput. Geosci. 60, 126–133.

Nichols, J.B., Voltolini, M., Gilbert, B., MacDowell, A.A., Czabaj, M.W., 2022. The hard x-ray nanotomography microscope at the advanced light source. Rev. Sci. Instrum. 93 (2).
Niwa, M., Mizuochi, Y., Tanase, A., 2015. Changes in chemical composition caused by water–rock interactions across a strike-slip fault zone: case study of the Atera fault, central Japan. Geofluids 15 (3), 387–409.
Pérez-López, R., Mediato, J.F., Rodríguez-Pascua, M.A., Giner-Robles, J.L., Ramos, A., Martín-Velázquez, S., Martínez-Orío, R., Fernández-Canteli, P., 2020. An active tectonic field for CO 2 storage management: the Hontomín onshore case study (Spain). Solid Earth 11 (2), 719–739.
Rezaee, M.R., Jafari, A., Kazemzadeh, E., 2006. Relationships between permeability, porosity and pore throat size in carbonate rocks using regression analysis and neural networks. J. Geophys. Eng. 3 (4), 370–376.
Shafaey, M.A., Salem, M.A.M., Ebied, H.M., Al-Berry, M.N., Tolba, M.F., 2018. Deep learning for satellite image classification. In: International Conference on Advanced Intelligent Systems and Informatics. Springer International Publishing, Cham, pp. 383–391.
Sibson, R., 1977. Fault rocks and fault mechanisms. J. Geol. Soc. 133, 191–213. London.
Sibson, R.H., 1994. Crustal stress, faulting and fluid flow. Geological Society, London, Special Publications 78 (1), 69–84.
Singla, A., Yuan, L., Ebrahimi, T., 2016. Food/non-food image classification and food categorization using pre-trained googlenet model. In: Proceedings of the 2nd International Workshop on Multimedia Assisted Dietary Management, pp. 3–11.
Smeraglia, L., Fabbi, S., Billi, A., Carminati, E., Cavinato, G.P., 2022a. How hydrocarbons move along faults: evidence from microstructural observations of hydrocarbon-bearing carbonate fault rocks. Earth Planet Sci. Lett. 584, 117454. https://doi.org/10.1016/j.epsl.2022.117454.
Smeraglia, L., Fabbi, S., Maffucci, R., Albanesi, L., Carminati, E., Billi, A., Cavinato, G.P., 2022b. The role of post-orogenic normal faulting in hydrocarbon migration in fold-and-thrust belts: insights from the central Apennines, Italy. Mar. Petrol. Geol. 136, 105429.
Szegedy, C., Liu, W., Jia, Y., Sermanet, P., Reed, S., Anguelov, D., Erhan, D., Vanhoucke, V., Rabinovich, A., 2015. Going deeper with convolutions. In: Proceedings of the IEEE Conference on Computer Vision and Pattern Recognition, pp. 1–9.
Voltolini, M., Ajo-Franklin, J., 2019. The effect of CO2-induced dissolution on flow properties in Indiana Limestone: an in situ synchrotron X-ray micro-tomography study. Int. J. Greenh. Gas Control 82, 38–47.
Wang, C., Li, P., Long, Q., Chen, H., Wang, P., Meng, Z., Wang, X., Zhou, Y., 2024. Deep learning for refined lithology identification of sandstone microscopic images. Minerals 14 (3), 275.
Wise, D.U., Dunn, D.E., Engelder, T., Geiser, P., Hatcher, R.D., Kish, S.A., Odom, L., Schamel, S., 1984. Fault-related rocks: suggestions for terminology. Geology 12, 391–394.
Woodcock, N.H., Mort, K., 2008. Classification of fault breccias and related fault rocks. Geol. Mag. 145, 435–440.
Worthington, S.R., 1999. A comprehensive strategy for understanding flow in carbonate aquifers. Karst modeling 35, 30–37.
Wu, G., Yang, H., He, S., Cao, S., Liu, X., Jing, B., 2016. Effects of structural segmentation and faulting on carbonate reservoir properties: a case study from the Central uplift of the tarim basin, China. Mar. Petrol. Geol. 71, 183–197.
Yilmaz, E., Trocan, M., 2021. A modified version of GoogLeNet for melanoma diagnosis. Journal of Information and Telecommunication 5 (3), 395–405.
Yuesheng, F., Jian, S., Fuxiang, X., Yang, B., Xiang, Z., Peng, G., Zhengtao, W., Shengqiao, X., 2021. Circular fruit and vegetable classification based on optimized GoogLeNet. IEEE Access 9, 113599–113611.
Zhang, Y., Wang, G., Li, M., Han, S., 2018. Automated classification analysis of geological structures based on images data and deep learning model. Applied Sciences 8 (12), 2493.
Zhiwen, D., Rujun, G., Fangfang, C., Jianping, Y., Zhongqian, Z., Zhimin, Y., Xiaohui, S., Bo, X., Erpeng, L., Tao, S., Chao, Z., 2020. Origin, hydrocarbon accumulation and oil-gas enrichment of fault-karst carbonate reservoirs: a case study of Ordovician carbonate reservoirs in south tahe area of halahatang oilfield, tarim basin. Petrol. Explor. Dev. 47 (2), 306–317.
Zhong, S., Zhang, K., Bagheri, M., Burken, J.G., Gu, A., Li, B., Ma, X., Marrone, B.L., Ren, Z.J., Schrier, J., Shi, W., 2021. Machine learning: new ideas and tools in environmental science and engineering. Environmental Science & Technology 55 (19), 12741–12754.